Journal of
Materials Chemistry A

PAPER

View Article Online
View Journal | View Issue

Cite this: *J. Mater. Chem. A*, 2025, **13**, 41390

A new strategy for balancing thermal stability and latent heat of solid–liquid PCMs *via* a solid–solid PCM as a supporting skeleton

Zhubin Yao,[a] Xiaoqing Yang,*[a] Xiaodong Lin,[a] Guoqing Zhang[a]
and Jingwen Weng*[b]

Received 5th July 2025
Accepted 23rd October 2025

DOI: 10.1039/d5ta05437k

rsc.li/materials-a

Insufficient thermal stability of phase change materials (PCMs) remains a fundamental limitation for next-generation battery thermal management. Here, we present a low-temperature skeleton-engineering strategy to construct a three-dimensional solid–solid phase change polymer (SSPCM) that immobilizes a solid–liquid PCM, yielding a composite PCM (CPCM) with exceptional thermal stability and application versatility. The SSPCM was formed by *in situ* free-radical copolymerization of stearyl acrylate (SA) and hexamethylene diacrylate (HA) as monomers within a paraffin matrix, using a redox initiation system. This process proceeds under mild conditions (as low as 40 °C), without requiring high temperature, pressure, or sealed environments, enabling a scalable and energy-efficient fabrication route. The resulting CPCM exhibits remarkable thermal stability, with a mass loss of only 0.35 wt% after 120 h at 55 °C (above its phase transition temperature), and retains structural integrity up to 250 °C. It also delivers a high latent heat of 112.02 J g^{-1} and a thermal conductivity of 2.36 W m^{-1} K^{-1}. When applied in lithium-ion battery modules, it significantly suppresses temperature rise, limiting the peak temperature to 49.1 °C and the temperature gradient to 1.82 °C under 2C discharge. This work offers a scalable, low-energy fabrication route to structurally stabilized PCMs, enabling multifunctional thermal management solutions in both energy storage and broader thermal control applications.

1 Introduction

The popularization and promotion of new energy vehicles (NEVs) is one of the effective ways to address the global challenges of energy depletion and environmental pollution.[1] With the continuous deepening of technological development, the market has put forward higher requirements for the performance of NEVs, such as higher range, superior power performance, and more reliable safety performance.[2] Notably, the achievement of these goals ultimately focuses on the core component of NEVs—the battery module.[3] At present, the battery modules used in NEVs are mainly lithium-ion batteries (LIBs),[4,5] and there is an inevitable problem with LIBs, which is that their performance is seriously affected by the working temperature.[6] It is generally believed that the safe working temperature range of LIBs is 25–50 °C, and the temperature difference between LIBs should not exceed 5 °C.[7] When the working temperature is excessively low, the mobility of lithium ions in the electrolyte is significantly retarded, manifesting as slower charging/discharging rates and reduced capacity.[8] However, when the working temperature is excessively high, the situation becomes even worse. Prolonged operation of LIBs in excessively high-temperature environments not only accelerates electrolyte decomposition, but also induces collapse of electrode material structures, loss of active materials, and permanent capacity reduction.[9] Over time, this will escalate internal side reactions, ultimately culminating in thermal runaway of the battery module. In response to the thermal safety hazards faced by LIB modules in NEVs, an efficient cooling system is recognized as a necessary configuration to ensure their safe operation.[10] In the early development stage of NEVs, air cooling was frequently adopted in battery thermal management systems (BTMs) for heat dissipation. Its simple structure, low cost, and easy maintenance make it suitable for small NEVs with low heat dissipation requirements or models with short range.[11] With the continuous development of NEVs, air cooling gradually cannot meet the heat dissipation needs due to its low heat dissipation efficiency.[12] Currently, automotive manufacturers such as BYD and Tesla have adopted liquid cooling BTM technology. Compared with air cooling BTM technology, liquid cooling BTM technology offers significantly higher heat dissipation efficiency.[13] However, liquid cooling systems inherently feature greater complexity and carry the risk of coolant leakage.[14] More critically, constrained by the overall design of the battery module, the liquid-cooled plates are typically

---

[a] *School of Materials and Energy, Guangdong University of Technology, Guangzhou 510006, PR China. E-mail: yangxiaoqing@gdut.edu.cn*

[b] *Department of Mechanical Engineering, Imperial College London, London SW7 2AZ, UK. E-mail: j.weng@imperial.ac.uk*

positioned at the module's bottom, which tends to exacerbate the internal temperature gradient within individual cells.[15]

In recent years, phase change material (PCM) BTM technology has received widespread attention.[16] As a passive heat dissipation technology, it combines the advantages of air cooling and liquid cooling BTM technology. While maintaining high heat dissipation efficiency and high temperature uniformity, it also has the characteristics of simple installation and maintenance. The PCMs mainly used in BTM technology are organic solid–liquid phase change materials (SLPCMs), such as paraffin, fatty acids, and fatty alcohols, which have high latent heat (170–250 J g^{-1}) and suitable phase change temperature (30–60 °C).[17] However, the inherent drawbacks of organic SLPCMs, primarily low thermal conductivity and weak thermal stability, are the main issues limiting their further development.[18,19] Specifically, the low thermal conductivity of SLPCMs induces significant thermal lag, thereby hindering their ability to efficiently dissipate heat from thermal sources. The primary strategy to mitigate this issue is to composite carbon materials[20] (*e.g.*, graphene, carbon nanotubes, and expanded graphite), metal particles[21] (*e.g.*, nano copper and nano silver), or ceramic materials[22] (*e.g.*, boron nitride and silicon carbide) as thermal conductivity additives with SLPCMs to improve their thermal conductivity. More critically, the weak thermal stability of SLPCMs presents more formidable challenges compared to their low thermal conductivity. SLPCMs experience a solid-to-liquid phase transition when heated, and the volume of PCMs exhibits significant expansion.[23] In some severe cases, leaked phase change ingredients can contaminate and corrode equipment, and they can also cause equipment short circuits, posing greater safety risks.[24,25] In the reported strategies for improving the thermal stability of SLPCMs, there are mainly two types. One is to incorporate polymer materials[26–29] (*e.g.*, epoxy resin, styrene–ethylene–butylene–styrene (SEBS), and low-density polyethylene (LDPE)), porous carbon materials, or other porous materials[30–32] (*e.g.*, diatomite and metal–organic frameworks (MOFs)) into SLPCMs, improving the thermal stability of SLPCMs through the coating and capillary condensation adsorption effect of supporting materials. Although this strategy is relatively simple and can generally be achieved through melt blending or vacuum impregnation adsorption, it can also lead to a new problem. When aiming to significantly improve PCM thermal stability, the required content of supporting materials is usually above 40 wt%, which will seriously reduce the energy storage efficiency of PCMs.[33,34] Another approach is to prepare SSPCMs based on chemical reactions, fundamentally solving the problem of weak thermal stability of PCMs through intermolecular forces. However, SSPCMs represented by polyurethane (obtained by crosslinking through –OH and –CNO groups) still have the drawback of low latent heat[35,36] (most SSPCMs have a latent heat of 50–80 J g^{-1}). In addition, as shown in Table 1, the reaction conditions for preparing SSPCMs are relatively complex, often requiring solvents, sealing, or oxygen-free conditions, and these requirements do not meet the conditions for large-scale preparation. Consequently, a lot of effort is still needed for the practical application of SSPCMs.

In summary, when using polymers or porous materials as the support skeleton for PCMs, there is a contradiction between improving thermal stability and reducing energy storage efficiency. Meanwhile, preparing SSPCMs through molecular synthesis also has the problems of low energy storage efficiency and overly complex preparation methods that are not suitable for batch production. To address the aforementioned issue, this work proposes a new strategy for balancing the thermal stability and energy density of PCMs. Specifically, expanded graphite (EG) serves as the thermal conductivity enhancer; paraffin (PA) serves as a phase change ingredient and reaction solvent; stearyl acrylate (SA) is used as the reactive monomer; hexamethylene diacrylate (HA) is used as the crosslinking agent, and benzoyl peroxide–*N*,*N*-dimethyl-*p*-toluene (BPO–DMPT) is used as the redox initiator system. SA and HA undergo *in situ* polymerization of C═C bonds in PA under the initiation of BPO-DMPT, constructing a 3D phase change polymer (corresponding to the SH-skeleton in the following manuscript) that simultaneously encapsulates PA and enhances thermal stability. The SH-skeleton not only has an adsorption function but also has a phase change function, which can effectively solve the problem of decreased energy density caused by the skeleton content. The latent heat of SH-skeleton is 99.55 J g^{-1}, and the latent heat of the composite PCM (corresponding to PESH–CPCM in the following manuscript) prepared with SH-skeleton, PA, and EG in mass fractions of 64 wt%, 30 wt% and 6 wt% is 112.02 J g^{-1}. As expected, the high skeleton content also endows PESH–CPCM with high thermal stability. For example, PESH–CPCM can maintain shape integrity at 250 °C, and the mass loss rate is only 0.35 wt% after heating at 55 °C for 120 h. In

Table 1 Preparation conditions required for partially reported SSPCMs

CPCM	Reaction temperature (°C)	Gas atmosphere	Solvent	Ref.
MHPCM	80	N_2	Yes	37
PPCM	80	N_2	No	38
PM	80	N_2	Yes	39
PEG-HDI-T	85	N_2	Yes	40
GO-g-PHDA	65	N_2	Yes	41
PAA-g-FA PCM	110	N_2	Yes	42
PEG/GO/h-BN	85	N_2	Yes	43
PU-SSPCM	60	N_2	Yes	44
PUPCM	70	N_2	Yes	45
PESH–CPCM	40	—	No	This work

addition, the SH-skeleton can be obtained at a reaction temperature of only 40 °C and does not require additional reaction conditions, such as oxygen free, water free or high-pressure environments, which creates conditions for its batch preparation. This study performed detailed chemical structure characterization and thermal property characterization of the prepared materials, and studied their applications in various fields, including thermal management in lithium-ion batteries and electronic device thermal management, solar cell thermal management, and photothermal conversion, confirming the enormous potential of PESH–CPCM.

2 Experimental section

2.1 Materials

SA (95%, Guangzhou Hongcheng Biochem Tech Co., Ltd); HA (80%, Shanghai McLean Biochem Tech Co., Ltd); BPO (AR, Shanghai McLean Biochem Tech Co., Ltd); DMPT (AR, Shanghai McLean Biochem Tech Co., Ltd); EG (50 mesh, Shanghai McLean Biochem Tec Co., Ltd); PA (AR, Guangzhou Zhongjia New Materials Tech Co., Ltd); epoxy resin (ER) (two-component type, epoxy value: 0.44 mol·(100 g)$^{-1}$, Shenzhen Mingde New Materials Co., Ltd). No further purification was performed on the reagents before use.

2.2 Preparation of PESH–CPCM and PEER–CPCM

A simple "one-pot method" was used to prepare PESH–CPCM. As shown in Fig. 1, first, 122.5 g SA and 60.0 g PA were weighed in a beaker and heated at 50 °C for 1 h to form a homogeneous solution. Subsequently, 12.0 g EG was slowly added to the mixed solution in batches, gradually increasing the speed of the stirrer (200–1000 r·min^{-1}). After all EG was added, the mixture was stirred at 1000 r·min^{-1} for 1 h until a uniform slurry was formed. Following this, 2.5 g HA and 2.9 g BPO were added sequentially and stirred for 30 min to facilitate complete dissolution of BPO. Finally, 0.5 g DMPT was added and stirred

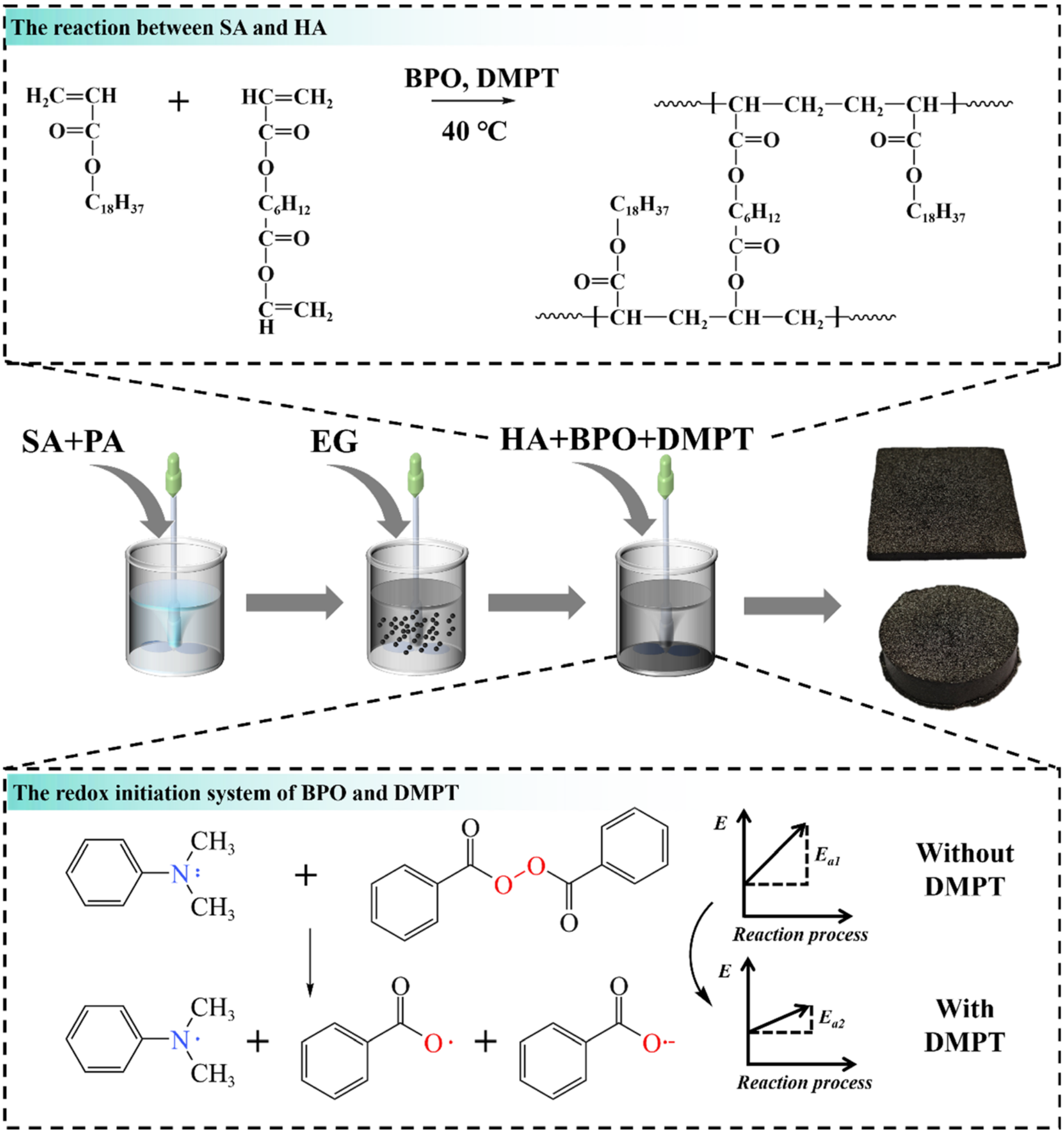

Fig. 1 Schematic diagram of PESH–CPCM preparation.

for 1 min until uniform, and the slurry was rapidly transferred into different customized molds and placed in an oven at 40 °C for 1 h to obtain PESH–CPCM. A cylindrical sample with dimensions of 30 mm (D) × 10 mm (H) was used for thermal stability testing. A rectangular sample with dimensions of 50 × 50 × 3 mm was used for thermal management of solar cells and electronic devices. The optimal ratio of SH-skeleton, PA, and EG was determined through preliminary experiments, and details can be found in the SI.

Only using BPO as the initiator for the C═C bond polymerization process typically requires a reaction temperature of 80–100 °C. In this work, DMPT was used as a reducing agent to undergo a redox electron transfer reaction with BPO, which could significantly reduce the decomposition activation energy of BPO and efficiently generate active free radicals ($PhCOO^•$) at temperatures as low as 40 °C, triggering the polymerization of C═C bonds.

To enable a direct performance comparison, ER without phase change capability was selected as the supporting skeleton to prepare the control group. Epoxy resin-based CPCM, comprising 55 wt% PA, 39 wt% ER, and 6 wt% EG, was prepared following our previous work,[46] which had a similar latent heat to PESH–CPCM. Specifically, 55 g PA and 19.5 g ER-part A were weighted in a beaker, and the mixture was heated at 60 °C for 1 h to form a uniform solution. Then, 6 g EG was slowly added in batches, and mechanically stirred for 1 h to obtain a uniform mixture. Finally, 19.5 g ER-part B was added, stirred for 3 min before pouring into the mold, and cured at room temperature for 24 h to obtain the CPCM, labeled as PEER–CPCM. The specific proportions of different samples are shown in Table 2.

2.3 Characterization

2.3.1 Chemical structure and microstructure characterization. A Fourier Transform Infrared Spectrometer (FTIR, Bruker Tensor II) was used to analyze the FTIR spectra of different materials, with spectra scanned in the wavenumber range of 500–4000 cm^{-1}. An X-ray diffractometer (XRD, Rigaku Ultima III) was used to analyze the XRD spectra of different materials, with a scanning angle range of 0–70° and a scanning rate of $10° \cdot min^{-1}$. Scanning electron microscopy (SEM, Hitachi TM3030) was used to test the microstructure of materials, with a 15 kV accelerating voltage.

2.3.2 Thermal property characterization. A thermal constant analyzer (Hotdisk 500) was used to analyse the thermal conductivity of different materials. Differential Scanning Calorimetry (DSC, METTLER DSC3) was employed to characterize the latent heat and phase change temperature of diverse materials, with a temperature range of 10–80 °C and a heating rate of 10 K min^{-1}, and 200 DSC cycles were performed under identical testing conditions. Simultaneous thermal analysis (TA Instruments-Waters LLC) was used to obtain the thermogravimetric (TG) curves of materials, within a temperature range of 50–800 °C and at a heating rate of 10 K min^{-1}. The thermal stability of PESH–CPCM and PEER–CPCM was analyzed through the following two sets of tests:

Group1: PESH–CPCM and PEER–CPCM were placed on a heating platform at 55 °C and heated for 120 h. The mass of the samples was measured every 12 h, and their mass loss rate was calculated using Formula (1):

$$M_{\text{loss}} = \left(\frac{M_i}{M_h} \div M_i\right) \times 100\% \tag{1}$$

In the formula, M_{loss} represents the mass loss rate of samples; M_i represents the initial mass of the samples; M_h represents the mass of the sample after heating.

Group2: PESH–CPCM and PEER–CPCM were placed on a heating platform and gradually heated from 30 °C to 250 °C. And their deformation and leakage performance at different temperatures were recorded by taking photographs.

2.3.3 Thermal management capability test

2.3.3.1 Thermal management testing of lithium-ion batteries. Initially, 18 650 ternary lithium-ion batteries were chosen as the research subjects (specific parameters are shown in Table 3), and the batteries and PESH–CPCM were assembled into battery modules. As shown in Fig. S3a, PESH–CPCM was cast into a rectangular module measuring 66 × 66 × 65 mm, with nine evenly spaced cylindrical holes (Φ 18 mm) embedded within the structure. Then, K-type thermocouples were attached to the surfaces of the batteries, and the batteries were then inserted into the corresponding holes of the PESH–CPCM module. Finally, nickel sheets were welded in a 3 series × 3 parallel configuration to form the battery module (15 Ah/10.8 V) for subsequent temperature control performance testing of the CPCM. The module assembled with PESH–CPCM and batteries was labeled as the PESH-module. In addition, the PEER-module with PEER–CPCM and the air-module without PCM were prepared in the same way.

Subsequently, as shown in Fig. S3b, a self-made experimental platform was used to analyze the temperature variations of the battery modules during charging–discharging cycles. Specifically, the battery module was equilibrated in a 25 °C constant temperature chamber before undergoing charging–discharging cycling. After that, the battery module was charged at 1C in constant current–constant voltage mode (CC–CV) and

Table 2 Specific composition of different samples

Sample	SSPCM-based cross-linked skeleton (wt%)	ER-based skeleton (wt%)	PA (wt%)	EG (wt%)
PESH–CPCM	64	—	30	6
SH-skeleton/PA	70	—	30	—
SH-skeleton	100	—	—	—
PEER–CPCM	—	39	55	6

Table 3 Specific parameters of the 26 650 cylindrical batteries used for testing

Parameters	Value or material
Cathode	$Li(Ni_5Co_2Mn_3)O_2$
Anode	Graphite
Electrolyte	$LiPF_6$
Rated capacity	5 Ah
Rated voltage	3.6 V

then discharged at 1C in constant current mode (CC). The interval between charging and discharging was 1 h, and the entire process was labeled as the 1C–1C single cycle test. In addition, the same charging–discharging mode was used to test the 1–2C and 1–3C single cycle tests, and 15 cycles of charging–discharging tests were conducted at 1–1.5C. During the testing process, an Agilent temperature date logger was used to record the temperature changes of the batteries.

2.3.3.2 *Thermal management testing of solar cells.* The CPCM was tightly attached to the back of the solar cell, and the solar cell was irradiated with a xenon lamp at a light intensity of 1.5 sun. At the same time, an Agilent temperature date logger and a direct-current electronic load were used to monitor the working temperature changes and output power of the solar cell during the irradiation process.

2.3.3.3 *Thermal management testing of electronic devices.* A ceramic heating element (CHE, 50 × 50 × 2 mm) was used to simulate the heating of electronic devices during operation. The CPCM was tightly attached to the back of the CHE, and a direct-current power supply was used to provide 4.5 W to the CHE. An Agilent temperature date logger and infrared thermal imaging devices were used to record the temperature changes of the CHE.

2.3.3.4 *Thermal conversion ability testing.* The PESH–CPCM was embedded in rubber insulation cotton, leaving only the front side exposed to receive light. Similarly, a xenon lamp was used to irradiate PESH–CPCM with a light intensity of 1.5 sun. The temperature change of the PESH–CPCM during the illumination process was recorded using an Agilent temperature date logger, and the photothermal conversion efficiency of PESH–CPCM was calculated using Formula (2):[47]

$$\eta = \frac{m\Delta H}{IS(t_i - t_0)} \tag{2}$$

In the formula, m represents the sample mass; ΔH represents the melting latent heat of CPCM; I represents the light intensity; S represents the irradiation area; t_0 and t_i represent the start time and end time of the phase change process, respectively.

3 Results and discussion

First, the prepared PESH–CPCM and SA were placed in toluene, as shown in Fig. 2a. It can be observed that SA completely dissolved in toluene after 24 h, while PESH–CPCM experienced

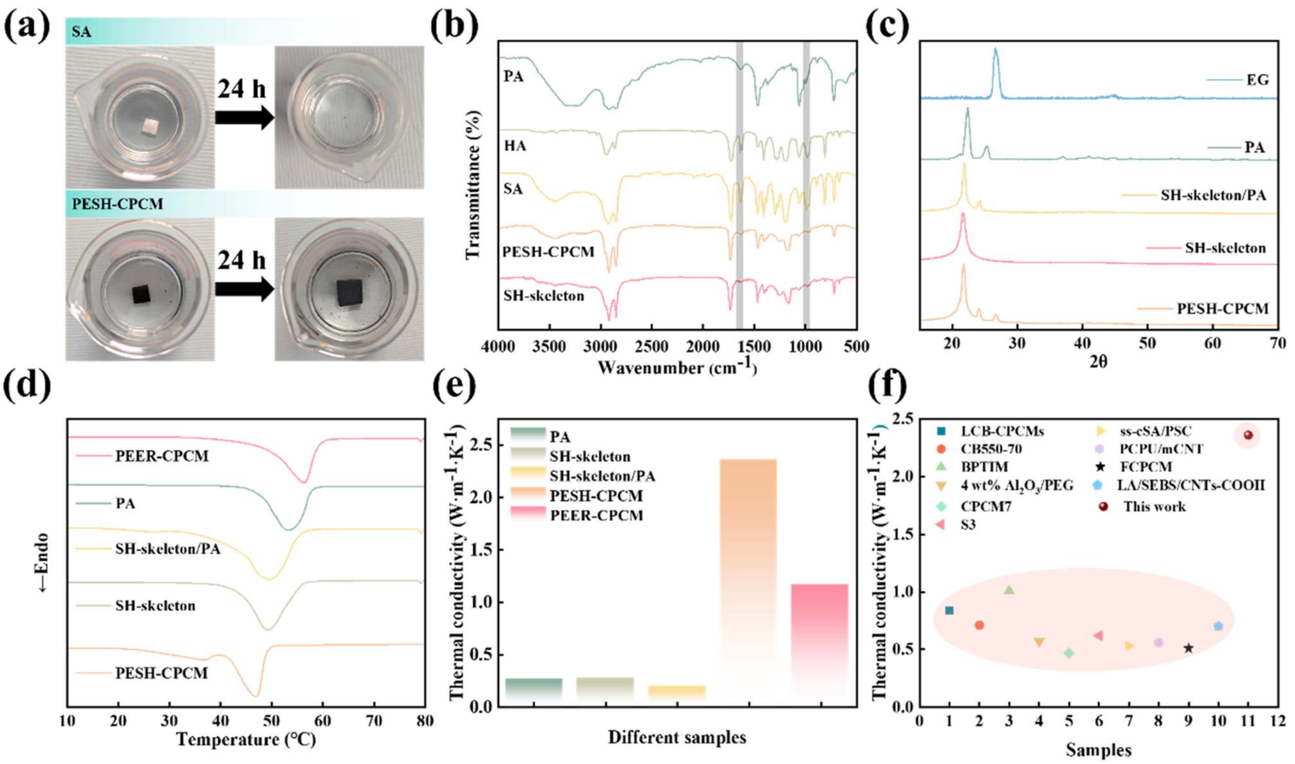

Fig. 2 (a) Dissolution experiments of SA and PESH–CPCM in toluene. (b) FTIR, (c) XRD, (d) DSC, and (e) thermal conductivity of different samples. (f) Comparison of thermal conductivity between this work and some reported studies: LCB-CPCMs;[48] CB550-70;[49] BPTIM;[50] 4 wt% Al_2O_3/PEG;[51] CPCM7;[52] S3;[53] ss-cSA/PSC;[54] PCPU/mCNT;[55] FCPCM;[56] LA/SEBS/CNTs-COOH.[19]

only swelling. This macroscopically confirms the successful aggregation of PESH–CPCM. To further demonstrate the successful synthesis of PESH–CPCM, the raw materials and PESH–CPCM were characterized by FTIR and XRD. In the FTIR curves of SA and HA (as shown in Fig. 2b), the characteristic peak at 1727 cm^{-1} is associated with the –C=O stretching vibration of the ester group, and the characteristic peaks at ∼1276 and ∼1195 cm^{-1} are associated with the –C–O– stretching vibration of the ester group. The characteristic peaks at the same position are also observed in the SH-skeleton, indicating the presence of ester groups in the SH-skeleton. In addition, the characteristic peak at 1467 cm^{-1} in the SH-skeleton is associated with the bending vibration of $-CH_2^-$, while the characteristic peak observed at 721 cm^{-1} is attributed to the bending vibration of $-(CH_2)_n^-$ ($n \geq 4$). More importantly, in the FTIR curves of SA and HA, the characteristic peak at around 1631 cm^{-1} is associated with the stretching vibration of C=C, while the characteristic peak at around 985 cm^{-1} is attributed to the bending vibration of C=C. These peaks are not observed in the SH-skeleton, which proves that SA and HA successfully underwent a polymerization reaction. Furthermore, the same C=C characteristic peak is not observed in PESH–CPCM, which further confirms that the addition of PA and EG does not affect the polymerization of the SH-skeleton. In the XRD curves shown in Fig. 2c, the characteristic diffraction peaks of PA at 25.3°, EG at 26.6°, and the SH-skeleton at 21.6° can all be observed in PESH–CPCM, which proves the uniform recombination between the SH-skeleton, EG, and PA. In addition, no additional characteristic diffraction peaks are observed in PESH–CPCM, which also proves that no chemical reaction occurs between the SH-skeleton, PA, and EG. The supporting skeleton in PESH–CPCM is also characterized. The SEM image of PESH–CPCM, labeled as PESH–CPCM (PA removed) after removing PA with dimethylbenzene, is shown in Fig. S4. It can be observed that after PA is removed, pore structures of 20–100 μm are distributed on the surface of PESH–CPCM, which can provide adsorption force for PA when PA transforms into the liquid phase.

The thermal management performance of PCMs is critically dependent on their thermophysical properties. Latent heat and thermal conductivity enable PCMs to absorb thermal energy more rapidly and efficiently, thereby improving their heat storage capacity and temperature regulation effectiveness. First, DSC was utilized to characterize the phase change behavior of PESH–CPCM, encompassing latent heat and phase transition temperature. As shown in Fig. 2d and Table 4, the measured latent heat of the SH-skeleton is only 99.55 J g^{-1}. However, the measured latent heat of PESH–CPCM can reach 112.02 J g^{-1}, which is approximately 12% higher than that of the SH-skeleton. And PESH–CPCM exhibits a suitable phase change temperature range of 40.5–48.9 °C, making it applicable for diverse thermal management scenarios. The thermal conductivity of various CPCMs is presented in Fig. 2e. When 6 wt% EG is incorporated, the thermal conductivity of PESH–CPCM reaches 2.36 W m^{-1} K^{-1}, which is 1080% greater than that of SH-skeleton/PA. This remarkable enhancement is primarily attributed to the continuous heat transfer skeleton formed by the uniform dispersion of EG within the SH-skeleton/PA matrix. Specifically, EG features a highly ordered graphite crystal structure with micron-scale lamellar morphology, which enables efficient phonon propagation with minimal scattering within its layers. This characteristic allows EG to serve as a "high-speed channel" for heat transfer, far outperforming the phonon propagation efficiency in the SH-skeleton/PA. As illustrated in Fig. 2f, the thermal conductivity of PESH–CPCM also remains comparatively high compared with most previously reported studies. Surprisingly, despite such a significant rise in thermal conductivity, the latent heat of PESH–CPCM is only reduced by 11% compared to SH-skeleton/PA. It is worth mentioning that compared to PEER–CPCM with the same EG content, PESH–CPCM has a higher thermal conductivity, which should be associated with the better compatibility between EG and SA, and the more dispersed EG forms a more continuous conductive skeleton. The addition of EG has significantly improved the thermal conductivity of PESH–CPCM, but it also introduces more defects that may lead to a decrease in the mechanical properties of PESH–CPCM. Regarding this, the strength of PESH–CPCM was evaluated through bending and compression mechanical performance tests, as shown in Fig. S5a and b. The calculated bending strength and compression strength of PESH–CPCM are 0.11 MPa and 10.98 MPa, respectively. In addition, a weighing experiment was conducted on PESH–CPCM, as shown in Fig. S5c. PESH–CPCM with a width of 13 mm and a thickness of 2.5 mm can carry a 200 g weight, while PESH–CPCM with a thickness of 4 mm can carry a 500 g weight. The twisting experiment of PESH–CPCM after heating at 40 °C is shown in Fig. S5d. When PESH–CPCM is heated, it exhibits better flexibility. This proves that when PESH–CPCM is applied to NEVs, it can more effectively mitigate vibrations generated during driving after absorbing the heat produced by the battery module during operation.

Table 4 Thermal characteristics of various samples

Samples	Phase change temperature (°C)	Latent heat (J g^{-1})	Thermal conductivity (W m^{-1} K^{-1})
PA	51.3	241.95	0.27
SH-skeleton	49.3	99.55	0.28
SH-skeleton/PA	46.9	120.63	0.20
PESH–CPCM	46.6	112.02	2.36
PEER–CPCM	56.3	116.83	1.17

The thermal stability of PCM, including shape stability and anti-leakage performance, is also a critical metric for measuring whether PCM has practical application potential. First, 200 DSC cycles of PESH–CPCM were tested at 10–80 °C, and the test results are displayed in Fig. 3a and b. And the latent heat of PESH–CPCM decreased from 112.7 to 112.1 J g^{-1} after 200 cycles, a decrease of only about 1%, which can be basically ignored. The cycle stability of PESH–CPCM is mainly attributed to the following aspects. Part of the latent heat in PESH–CPCM is provided by the SH-skeleton. Since the phase change segments (C18) in the SH-skeleton are chemically bonded to the cross-linked skeleton, this fundamentally eliminates the problem of leakage for the SH-skeleton. For the part of the latent heat provided by PA in PESH–CPCM, on one hand, during the preparation process, the polymerization of SA and HA to form the SH-skeleton occurs directly in PA, enabling the SH-skeleton to effectively encapsulate PA. On the other hand, according to reported studies, EG can also provide partial adsorption for PA.[57,58] Furthermore, microscopically, the phase change segments (C18) of the SH-skeleton and the alkane segments composing PA are entangled with each other, and the van der Waals forces between the segments further enhance the cycle stability of PESH–CPCM. The TG curves of PA, SH-skeleton, and PESH–CPCM are shown in Fig. S6. The decomposition temperature of PA in PESH–CPCM is about 200 °C. Compared with pure PA, PA in PESH–CPCM has a slower decomposition rate. This is one of the pieces of evidence that the supporting skeleton constructed by the SH-skeleton and EG provides adsorption force for liquid-phase PA.

To better evaluate the thermal stability of PESH–CPCM, continuous heating and high-temperature impact experiments were conducted on PESH–CPCM and PEER–CPCM. First, PESH–CPCM and PEER–CPCM were placed on a heating platform at 55 °C for 120 h. The test results are presented in Fig. 3c. After long-term heating, the M_{loss} of PESH–CPCM is only 0.35 wt%, while the M_{loss} of PEER–CPCM is as high as 8.02 wt%. In the high-temperature impact experiment, as shown in Fig. 3d, PESH–CPCM and PEER–CPCM were positioned on a heating platform and heated from 30 °C to 250 °C. By observing the leakage behavior and shape change of PESH–CPCM and PEER–CPCM at different temperatures, it was found that PEER–CPCM exhibited leakage performance when the temperature rose to 70 °C. As the temperature increased, the leakage performance continued to worsen. In contrast, PESH–CPCM showed no detectable leakage until approximately 200 °C. The reason why PESH–CPCM has better thermal stability than PEER–CPCM is twofold: on the one hand, there are molecular dispersion forces between the alkane side chains (C18) in the SH-skeleton and the straight chain alkanes in PA. On the other hand, the 3D network structure of the SH-skeleton could restrict the molecular chains of PA effectively.

In order to better understand the phase change crystallization behavior of the SH-skeleton and PESH-CPCM, as well as their effects on thermal stability and other properties, a polarizing optical microscope (POM) was used to characterize the crystal morphology of the SH-skeleton and PESH–CPCM and DSC was used to analyze their crystallization kinetics. As shown in Fig. S7a and b, the POM images of the SH-skeleton and PESH–CPCM reveal a fragmented distribution of their

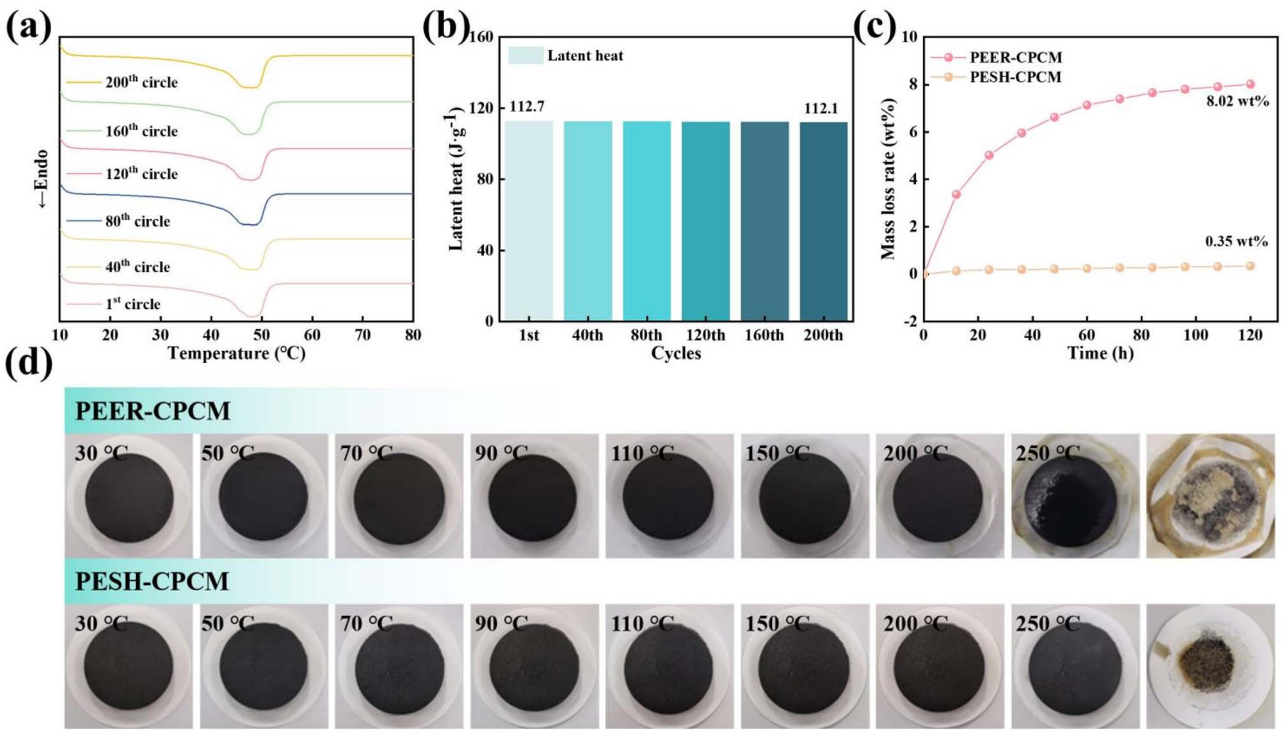

Fig. 3 (a) 200 DSC cycles of PESH–CPCM and (b) calculated latent heat. (c) The mass loss rate of PESH–CPCM and PEER–CPCM during heating at 55 °C for 120 h. (d) Leakage performance and shape changes of PESH–CPCM and PEER–CPCM during the heating process at 30–250 °C.

crystalline regions, potentially attributed to the side-chain crystallization behavior of the SH-skeleton. The molecular chain of the SH-skeleton is composed of a rigid amorphous main chain and flexible crystallizable side chains (C18), and its crystallization process is independently completed by C18.[59] C18 folds into a lamellar structure through intermolecular van der Waals forces, forming small crystalline aggregates, which correspond to bright regions in POM; while the main chain skeleton forms amorphous regions due to its rigid network structure, corresponding to dark regions in POM. This further provides evidence for why the SH-skeleton has latent heat.

Next, the non-isothermal crystallization kinetics of the SH-skeleton and PESH–CPCM were analyzed, and the activation energy (E_a) of the energy barrier during the crystallization process was calculated based on the Kissinger equation:[60–62]

$$\ln\frac{\varphi}{{T_p}^2} = -\frac{E_a}{R}\times\frac{1}{T_p} + \ln\left(\frac{A\times R}{E_a}\right) \quad (3)$$

In the formula, φ represents the cooling rate; T_p is the peak temperature during the crystallization process; E_a is the activation energy used to characterize the energy barrier that needs to be overcome during the crystallization process; A is the frequency factor, which is a parameter that characterizes the crystallization rate; R is the gas constant, with a value of 8.314 $\text{J}\cdot(\text{kg K})^{-1}$.

The non-isothermal DSC curves of the SH-skeleton and PESH–CPCM are shown in Fig. S7c and d, and the parameters obtained based on T_p are recorded in Table S3. Linear fitting was performed on the obtained $1/T_p$ and $\ln(1/{T_p}^2)$ to obtain E_a from the slope. As shown in Fig. S7e and f, the E_a values of the SH-skeleton and PESH–CPCM are 151.28 kJ mol^{-1} and 204.19 kJ mol^{-1}, respectively. Compared to the SH-skeleton, PESH–CPCM requires a larger E_a during the crystallization process. This is presumably due to EG being dispersed as a rigid filler in the SH-skeleton matrix, forming a physical barrier that hinders the diffusion of the side chains (C18) of the SH-skeleton and the molecular chains of PA. Additionally, the steric hindrance significantly increases, leading to an increase in E_a of PESH–CPCM. The magnitude of E_a directly reflects the rate of crystallization kinetics. Specifically, a higher E_a means that PESH–CPCM requires more energy to overcome spatial hindrance and form regular chain segment arrangements, which slows down crystal nucleation and manifests as lower crystallinity. And lower crystallinity implies weaker intermolecular forces—a factor that also contributes to PESH–CPCM having a lower phase change temperature than the SH-skeleton. This also indirectly reflects that the thermal stability of PESH–CPCM is lower than that of the SH-skeleton.

Overall, owing to its high latent heat (112.02 J g^{-1}), favorable phase change temperature span (40.5–48.9 °C), high thermal conductivity (2.36 W m^{-1} K^{-1}), and exceptional thermal stability, PESH–CPCM exhibits notable potential for practical applications. To validate its feasibility in lithium-ion battery thermal management, as shown in Fig. 4a–f and Table 5, three battery modules (PESH-module, PEER-module, and air-module) were prepared and tested at varying charging–discharging rates. The maximum temperature (T_{max}) of the entire battery module was represented by the temperature of the central battery, while the maximum temperature difference (ΔT_{max}) was calculated by the difference between the central battery and the edge battery. As shown in Fig. 4a, the three different battery modules have similar maximum temperatures at a 1C–1C rate. Owing to the low heat generation at a discharge rate of 1C, the temperature of the battery has not yet entered the phase change temperature range of the CPCMs. In this instance, natural air cooling still plays a role in heat dissipation. In addition, Fig. 4b shows the ΔT_{max} corresponding to the three modules. It can be found that the ΔT_{max} of the air-module reaches 3.64 °C, while the ΔT_{max} of the PESH-module and the PEER-module is only 0.74 °C and 2.03 °C respectively, indicating that the CPCM not only provides temperature control, but also has good temperature equalization performance. It is worth mentioning that the higher thermal conductivity of the PESH-module compared to the PEER-module accelerates heat transfer, resulting in lower ΔT_{max} in the PESH-module. When the discharge rate is 2C, as shown in Fig. 4c and d, the T_{max} and ΔT of the three modules increase to varying degrees compared to the 1C discharge rate. The T_{max} and ΔT_{max} of the PESH-module, PEER-module, and air-module are 49.1 & 1.82 °C, 51.9 & 3.27 °C, and 61.6 & 6.45 °C, respectively. Furthermore, as shown in Fig. 4e and f, when the discharge rate is increased to 3C, it is found that the T_{max} and ΔT_{max} of the air-module reach up to 77.6 °C and 9.03 °C after the discharge is completed. The T_{max} and ΔT_{max} far exceed the safe operating range of the battery, which means that the risk of thermal runaway in the battery module is greatly increased. However, owing to the instantaneous thermal regulation of CPCM, both the PESH-module and PEER-module exhibit controlled T_{max} values of 54.7 °C and 57.8 °C respectively, with corresponding ΔT_{max} maintained at 4.34 °C and 5.39 °C, which are much lower than those of the air-module. In addition, as shown in Fig. 4g and h, to further verify the temperature control stability of PESH–CPCM, cycle testing at 1C–1.5C was conducted for 15 cycles. The T_{max} and ΔT_{max} of the PESH-module during the 15 charging–discharging cycles are 52.3 and 4.23 °C, which are lower than those of the PEER-module (55.1 & 4.61 °C). The results of the cycle test are consistent with those of the single charging–discharging test.

Thermal effects pose significant challenges not only to battery performance but also to electronic systems, where heat accumulation critically impacts operational stability and device longevity. Using PCMs to dissipate heat from electronic devices is one of the effective methods. In this work, PESH–CPCM was tightly attached to the ceramic heating element (CHE) through thermal conductive silicone grease, labeled as PESH-CHE. Similarly, CHE with PEER–CPCM is labeled as PEER-CHE, while CHE without phase change materials was labeled as Air-CHE. Fig. 5a and b show the infrared thermal images and temperature variation curves of different samples at a heating power of 4.2 W. For Air-CHE, after heating for 15 min, the temperature rises to 74.7 °C. Conversely, the temperature curves of PESH-CHE and PEER-CHE show a clear temperature plateau, corresponding to the latent heat absorption of CPCM. The highest temperatures of PESH-CHE and PEER-CHE decrease to

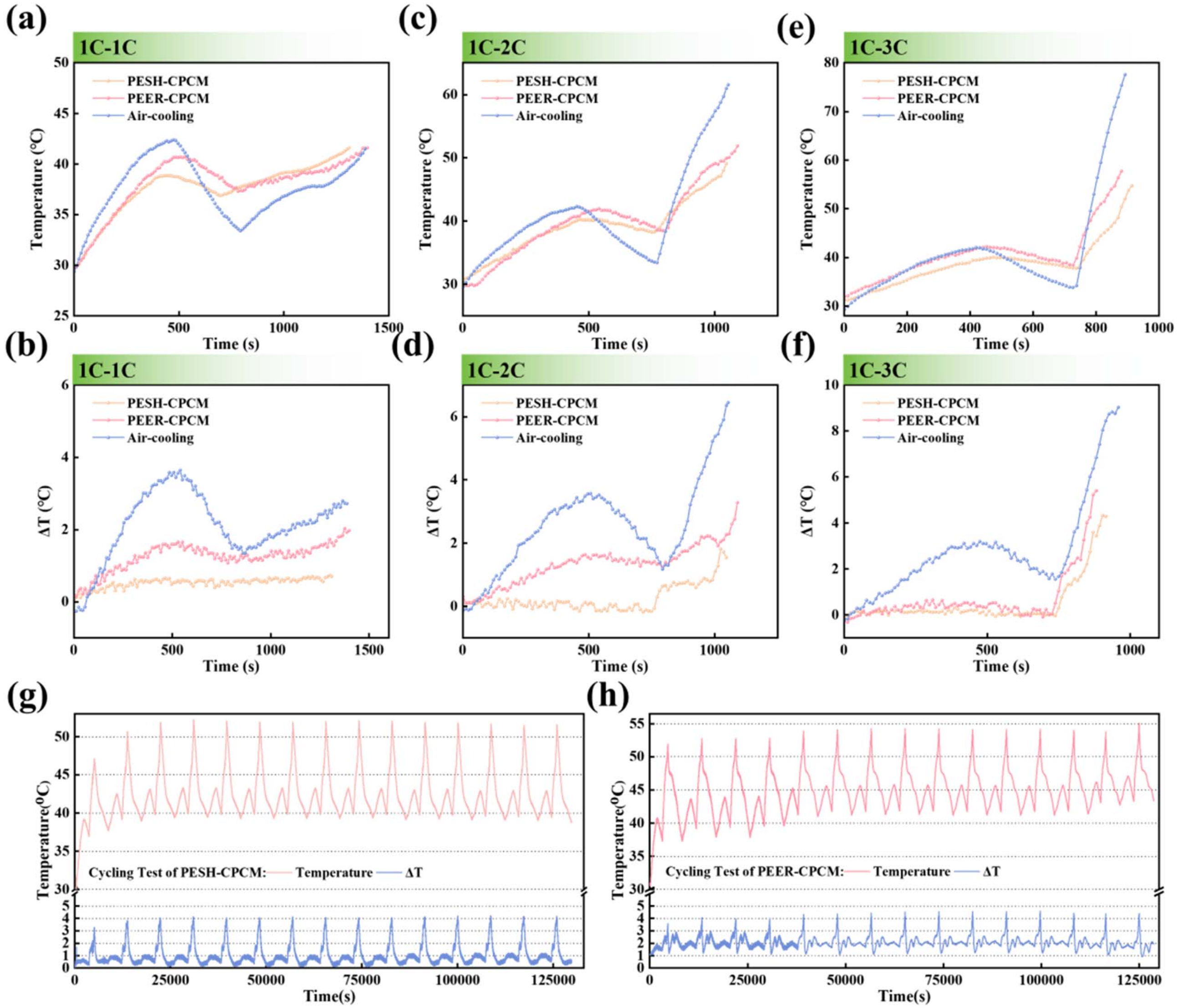

Fig. 4 Temperature variation curves (a) and temperature difference variation curves (b) of different battery modules at a 1C discharge rate. Temperature variation curves (c) and temperature difference variation curves (d) of different battery modules at a 2C discharge rate. Temperature variation curves (e) and temperature difference variation curves (f) of different battery modules at a 3C discharge rate. (g) Temperature and ΔT curves of PESH–CPCM at a 1.5C discharge rate for 15 cycles. (h) Temperature and ΔT curves of PEER–CPCM at a 1.5C discharge rate for 15 cycles.

varying degrees compared to Air-CHE, with PESH-CHE showing a more significant decrease in temperature. Specifically, the highest temperature of PESH-CHE is 57.0 °C, which decreases by 17 °C compared to Air-CHE. This is also attributed to the higher thermal conductivity of PESH–CPCM.

The in-depth study of PCM is also of great significance for the utilization of solar energy. Reported research shows that the output power of solar cells decreases 0.4–0.5% for every 1 °C increase in temperature,[63] and it is necessary to carry out thermal management of solar cells to improve their power generation. In the simulation test of solar cell thermal management, PESH–CPCM and PEER–CPCM were tightly attached to the back of the solar cell, and xenon lamps were used to simulate solar radiation at an intensity of 1.5 sun. At the

Table 5 T_{max} and ΔT_{max} at various charging–discharging rates

	1C–1C		1C–2C		1C–3C		15 cycles of 1C–1.5C	
	T_m (°C)	ΔT_{max} (°C)	T_m (°C)	ΔT_{max} (°C)	T_m (°C)	ΔT_{max} (°C)	T_m (°C)	ΔT_{max} (°C)
PESH-module	41.6	0.74	49.1	1.82	54.7	4.34	52.3	4.23
PEER-module	41.6	2.03	51.9	3.27	57.8	5.39	55.1	4.61
Air-module	42.4	3.64	61.6	6.45	77.6	9.03	—	—

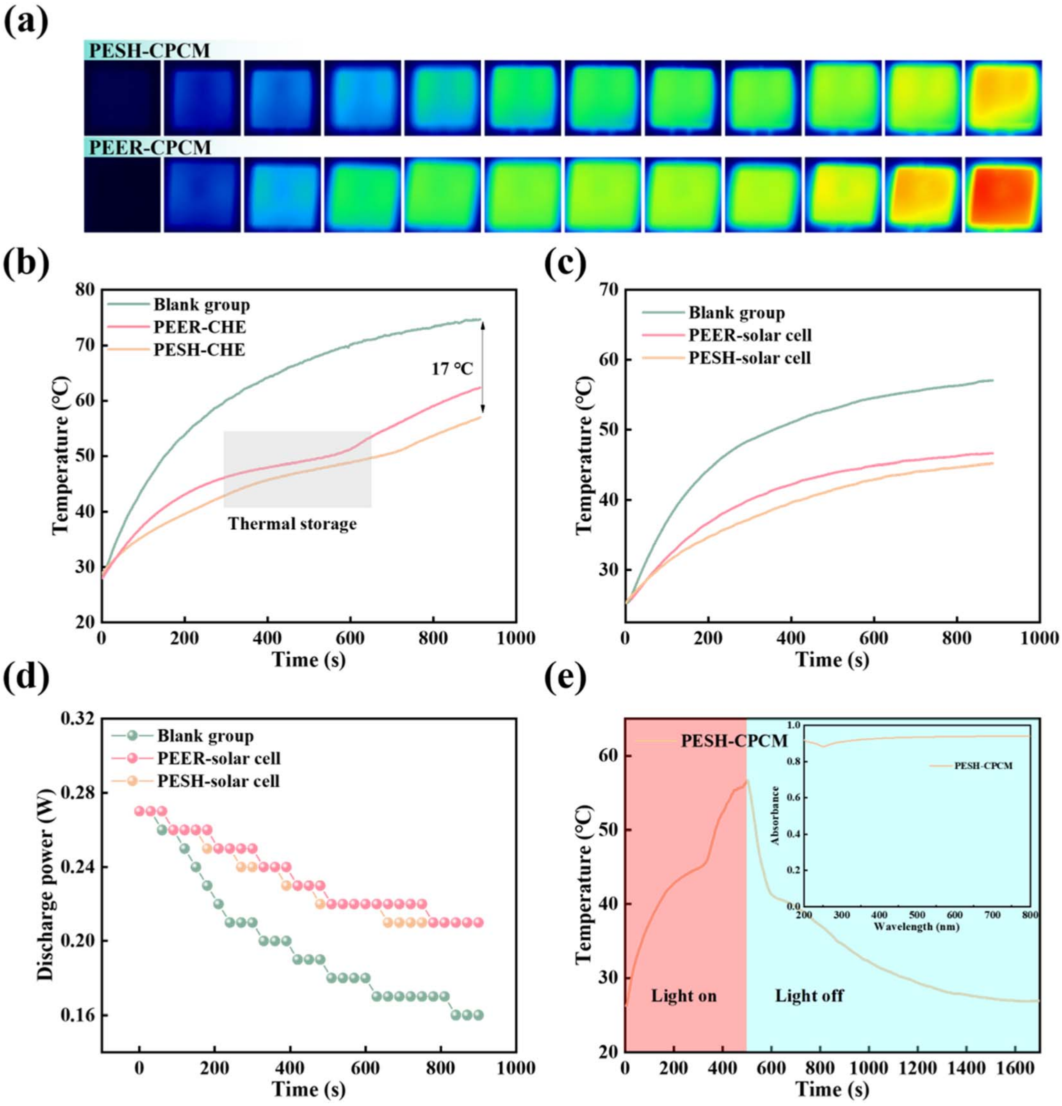

Fig. 5 The infrared thermal images (a) and temperature variation curves (b) of different samples at a heating power of 4.2 W. The temperature variation curve (c) and output power variation (d) of SH-skeleton-solar cells and SLPCM-solar cells under 1.5 sun. (e) The temperature variation curve of PESH–CPCM under 1.5 sun.

same time, an Agilent temperature date logger and direct-current electronic load were used to record the temperature changes and output power changes of the solar cell during the irradiation process. The groups used for testing were labeled as PESH-solar cell, PEER-solar cell, and blank group (without CPCM). Fig. 5c and d show the temperature variation curves and output power changes during the irradiation process. After 900 s of irradiation, the temperature of the blank group increases to 57.1 °C, and the corresponding output power of solar energy decreases from 0.27 W to 0.16 W. However, the highest temperatures of PESH-solar cells and PEER-solar cells show a significant decrease compared to the blank group, reaching 45.2 and 46.4 °C, respectively. Correspondingly, their output power also has a higher retention rate after irradiation, decreasing from 0.27 W to 0.21 W. This simulation experiment proves that PESH–CPCM can significantly improve the power generation of solar cells by reducing the temperature during irradiation.

Finally, the photothermal conversion efficiency of PESH–CPCM was evaluated. The UV-visible absorption spectra of PESH–CPCM were tested first, as shown in Fig. 5e. Within the UV-visible wavelength range of 200–800 nm, PESH–CPCM exhibits high absorption rates. Fig. 5e also shows the temperature change of PESH–CPCM under 1.5 sun. It can be observed that the temperature continuously rises and a plateau of slow temperature increase appears, corresponding to the phase change endothermic process. After the illumination ends, the temperature begins to decrease and a plateau of slow temperature decrease also appears, corresponding to the crystallization exothermic process of PESH–CPCM. Using the photothermal conversion efficiency Formula (2), the photothermal conversion efficiency of PESH–CPCM is calculated to be

81.2%, indicating that PESH–CPCM not only has excellent heat dissipation ability, but also has considerable photothermal conversion ability.

4 Economic and energy investment evaluation of large-scale preparation of PESH–CPCM

The evaluation of raw material costs and energy input for large-scale preparation of PESH-CPCM is one of the necessary conditions for industrialization. First, the costs of various industrial-grade raw materials used in the preparation of PESH–CPCM were investigated, as shown in Table S4. The cost of PESH–CPCM, formulated with 61.15 wt% SA, 30.00 wt% PA, and 6.00 wt% EG, 1.25 wt% HA, 1.45 wt% BPO, and 0.15 wt% DMPT, is approximately 6.06 $\text{USD}\cdot\text{kg}^{-1}$, which demonstrates the economic viability of PESH–CPCM in terms of raw material costs. And if the production of PESH–CPCM can become a complete and mature industrial chain, we believe that its raw material costs can be further reduced.

For the energy input in the preparation process of PESH-CPCM, we calculated the energy required for preparing 1 kg PESH–CPCM under laboratory conditions. As shown in Fig. S8a–c, the equipment used in the preparation process includes an oil bath (Shanghai Lichen Technology Instrument Co., Ltd; input power: 0.6 kW), a mechanical stirrer (Changzhou Surui Instrument Co., Ltd; input power: 0.12 kW), and an incubator (Shanghai Yiheng Scientific Instrument Co., Ltd; input power: 1.45 kW). In this preparation process, the working time of the oil bath is approximately 2.5 h; the working time of the stirrer is approximately 1 h, and the working time of the incubator is approximately 1 h. The calculated energy input for preparing 1 kg PESH–CPCM in the laboratory is approximately 3.07 kWh kg^{-1}. On this basis, we also investigated the commonly used mixing and heating equipment and incubators in industrial production, such as the dual planetary mixer (Wuxi Baowoleke Technology Co., Ltd, 100 L, input power: 20 kW) and the industrial grade incubator (Guangdong Jianda Intelligent Equipment Co., Ltd, 408 L, input power: 7.5 kW), as shown in Fig. S8d and S8e. A dual planetary mixer can prepare approximately 100 kg PESH–CPCM each time, with an energy input of approximately 0.58 kWh kg^{-1}. It can be observed that the energy input in the preparation process of PESH–CPCM significantly decreases with increasing preparation scale. We believe that with the further expansion of the preparation scale, the energy input will further decrease. In summary, we believe that PESH–CPCM has economic feasibility in terms of raw materials and energy input for large-scale preparation through calculation and analysis, and PESH–CPCM has potential for industrial production.

5 Conclusion

This work proposes a new solution to overcome the long-standing trade-off between thermal stability and energy storage density in composite phase change materials (CPCMs). By introducing a redox initiation system with this novel approach, SA and HA were successfully polymerized *in situ* within PA at just 40 °C, forming a dual-functional SH-skeleton. This dual-functional SH-skeleton not only serves as a robust structural framework for PA but also contributes 99.55 J g^{-1} of latent heat, synergistically enhancing energy storage capacity. The obtained PESH–CPCM composite exhibits outstanding energy storage characteristics with a latent heat of 112.02 J g^{-1} and a thermal conductivity of 2.36 W m^{-1} K^{-1}, demonstrating exceptional applicability in thermal regulation systems for lithium-ion batteries, solar cells, and electronic devices. Further leveraging EG's superior light absorption properties, PESH–CPCM achieves a photothermal conversion efficiency of 81.2%, positioning it as a promising candidate for solar energy harvesting systems. Noteby, PESH–CPCM can maintain shape integrity at 250 °C without detectable deformation, and after 120 h of thermal aging at 55 °C, the quality loss remains below 0.35%, demonstrating excellent thermal stability. In summary, this work establishes a paradigm-shifting methodology for developing high-stability CPCMs through *in situ* low-temperature polymerization. The successful integration of energy storage, thermal regulation, and photothermal conversion functionalities not only addresses current limitations in thermal energy systems but also opens new pathways for sustainable energy utilization.

Author contributions

Zhubin Yao: conceptualization, investigation, data curation, software, writing – original draft. Xiaoqing Yang: supervision, methodology, resources, writing – review & editing, project administration. Xiaodong Lin: investigation, data curation. Guoqing Zhang: supervision, validation. Jingwen Weng: supervision, methodology, writing – review & editing, project administration.

Conflicts of interest

There are no conflicts to declare.

Data availability

All data supporting the findings of this study, including thermal analysis data, structural characterization, and simulation outputs, are provided in the supplementary information (SI) and can be shared upon request after publication. No additional datasets or code were deposited in public repositories.

Supplementary information is available. See DOI: **https://doi.org/10.1039/d5ta05437k**.

Acknowledgements

The authors gratefully acknowledge the financial support from the Natural Science Foundation of Guangdong Province (2024A1515012472, 2025A1515011548) and the European Commission through the Marie Skłodowska-Curie Actions (Grant No. 101206935).

References

1 R. Guo, Z. Y. Sun and M. H. Luo, *Energy*, 2024, **307**, 132769.

2 T. Y. Wang, J. Wu, J. W. Wu, C. T. Li, B. Q. Lu, J. P. Chen and J. Y. Shi, *Appl. Therm. Eng.*, 2025, **269**, 126002.

3 A. Farakhor, D. Wu, Y. B. Wang and H. Z. Fang, *Ieee T Transp Electr*, 2024, **10**, 5002–5016.

4 L. Cong, W. H. Wang and Y. Wang, *J. Energy Storage*, 2024, **94**, 112406.

5 M. Mama, E. Solai, T. Capurso, A. Danlos and S. Khelladi, *Energy Convers. Manage.*, 2025, **325**, 119223.

6 Y. F. Li, C. Jiang, C. G. Zhao, D. H. Zhu, L. L. Wang, H. Q. Xie and W. Yu, *Renewable Sustainable Energy Rev.*, 2025, **216**, 115706.

7 J. J. Wang, Y. Yu, L. F. Song, Y. B. Yue, W. Zeng, W. X. Mei and Q. S. Wang, *Energy Convers. Manage.*, 2024, **302**, 118106.

8 K. Chen, J. Y. Luo and Y. Q. Huang, *Chem. Eng. J.*, 2025, **503**, 158260.

9 X. Y. He, Y. H. Ling, Y. H. Wu, Y. Lei, D. W. Cao and C. L. Zhang, *Small*, 2025, 2412817.

10 X. Y. Li and R. Z. Wang, *Etransportation*, 2025, **24**, 100396.

11 A. Gharehghani, M. Rabiei, S. Mehranfar, S. Saeedipour, A. M. Andwari, A. García and C. M. Reche, *Renewable Sustainable Energy Rev.*, 2024, **202**, 114654.

12 D. Luo, Y. Zhao, J. Cao, W. H. Chen, Y. L. Zhao and B. Y. Cao, *Renewable Energy*, 2024, **224**, 120193.

13 E. Pilali, M. Soltani, M. Hatefi, S. Shafiei, M. Salimi and M. Amidpour, *J. Power Sources*, 2025, **632**, 236345.

14 P. Ganeshkumar, V. Sivalingam, S. Divya, T. H. Oh, V. S. Vigneswaran and R. Velraj, *J. Energy Storage*, 2024, **87**, 111412.

15 K. Shen, J. Y. Sun, Y. J. Zheng, C. S. Xu, H. B. Wang, S. Y. Wang, S. Q. Chen and X. N. Feng, *Appl. Therm. Eng.*, 2022, **211**, 118422.

16 Q. Q. Huang, X. X. Li, J. Deng, W. S. Yang, Y. Y. Zeng, Z. H. Rao, F. L. Kong and Y. L. Li, *Energy Storage Mater.*, 2025, **80**, 104344.

17 V. V. Tyagi, K. Chopra, R. K. Sharma, A. K. Pandey, S. K. Tyagi, M. S. Ahmad, A. Sari and R. Kothari, *Sol. Energy Mater. Sol. Cells*, 2022, **234**, 111392.

18 X. Zhang, L. Geng, G. Y. Liang, H. L. Gan, Y. T. Cao, G. Li, Y. X. Lin, J. T. Zhao and C. H. Liu, *J. Energy Storage*, 2025, **113**, 115617.

19 Z. C. Li, Y. Zhang, X. Wang, X. Y. Guo, S. F. Zhang and B. T. Tang, *J. Power Sources*, 2024, **603**, 234447.

20 X. X. Zeng, L. S. Ye, C. H. Wang, D. E. Wu, K. W. Zhong and Z. J. Kong, *J. Energy Storage*, 2024, **88**, 111495.

21 D. G. Atinafu, B. Y. Yun, S. Wi, S. J. Chang and S. Kim, *J. Energy Storage*, 2023, **60**, 106650.

22 J. B. Xiao, B. Zou, F. F. Zhong, C. H. Liu, W. Y. Qiao, M. Ding and C. K. Jia, *Appl. Therm. Eng.*, 2024, **257**, 124182.

23 J. Lamotte-Dawaghreh, J. Herring, R. Bhandari, A. Lakshminarayana, R. Suthar, P. Bansode, D. Agonafer, N. Ramos, N. Teufel, T. Silvers, M. Wilson, D. Eifert and D. Martorana, *Heat Transf Res*, 2024, **55**, 59–79.

24 S. J. Han, J. P. Li, J. Zang, Q. Y. Ding, Z. C. Yu and Y. Lu, *Int. J. Biol. Macromol.*, 2025, **287**, 138655.

25 Y. Han, Q. He, Y. Q. Fang, J. K. Nie, W. N. Qin, H. Liu and K. Zhu, *ACS Appl. Polym. Mater.*, 2025, **7**, 5339–5347.

26 H. J. M. Pea, Z. J. An, X. Z. Du, B. A. Fu, D. Zhang and X. Z. Wang, *Chem. Eng. J.*, 2024, **490**, 151558.

27 Y. G. Jing, Z. C. Zhao, X. L. Cao, Q. R. Sun, Y. P. Yuan and T. X. Li, *Nat. Commun.*, 2023, **14**(1), 8060.

28 G. H. Wu, J. Q. Shen, S. R. Huang, Z. M. Zhang, Y. J. Li and L. J. Ye, *ACS Appl. Polym. Mater.*, 2025, **7**, 5519–5527.

29 K. Y. Chan, X. L. Dong, Y. F. Yang, X. M. Zhao, D. Li, M. Y. Xu, X. M. Yin, Z. Y. Wang and X. Shen, *Mater. Horiz.*, 2025, **12**, 5175–5186.

30 C. Chang, B. Li, B. C. Fu, X. Yang and Y. L. Ji, *Polymers*, 2023, **15**(24), 4723.

31 S. L. Wang, Q. Huang, Z. H. Sun, Y. H. Wang, T. X. Liang, B. G. Wang, C. F. Fan and C. C. Liu, *Carbon*, 2024, **226**, 119174.

32 Y. Ma, H. Yang, H. Y. Zuo, Y. Ma, Q. S. Zuo, Y. Chen, X. X. He and R. R. Wei, *Energy*, 2023, **278**, 127798.

33 W. X. Luo, X. W. Hu, Y. H. Che, S. Zu, Q. L. Li, X. X. Jiang and D. J. Liu, *J. Energy Storage*, 2022, **52**, 105060.

34 C. Q. Zhu, Y. K. Chen, R. S. Cong, F. M. Ran and G. Y. Fang, *Sol. Energy Mater. Sol. Cells*, 2021, **219**, 110782.

35 Y. Y. Yang, W. B. Kong and X. F. Cai, *Energy Build.*, 2018, **158**, 37–42.

36 J. M. Chang, H. Y. Lu, Y. L. Xiao, S. Wu, Y. Xiao and Y. C. Wang, *J. Appl. Polym. Sci.*, 2024, **141**(7), 54950.

37 C. Y. Wang, X. Geng, J. Chen, H. L. Wang, Z. K. Wei, B. X. Huang, W. Liu, X. D. Wu, L. Y. Hu, G. H. Su, J. X. Lei, Z. M. Liu and X. He, *Adv. Mater.*, 2024, **36**(11), 2309723.

38 B. Wu, Z. Liu, Y. Xiao, Y. Wang, C. Zhou, X. Zhang and J. Lei, *J. Appl. Polym. Sci.*, 2018, **136**(9), 47108.

39 S. Sundararajan, A. B. Samui and P. S. Kulkarni, *React. Funct. Polym.*, 2018, **130**, 43–50.

40 L. Li, J. Peng, L. Wang, J. Lai, C. Zhao, D. Xiang, H. Li, G. Yan, Z. Li and Y. Wu, *J. Mater. Chem. A*, 2025, **13**, 3073–3083.

41 R. Cao, H. Liu, S. Chen, D. Pei, J. Miao and X. Zhang, *Compos. Sci. Technol.*, 2017, **149**, 262–268.

42 E. Bastürk and M. V. Kahraman, *Polym.-Plast. Technol.*, 2018, **57**, 276–282.

43 R. Jing, H. Z. Zhang, C. W. Huang, F. C. Su, B. J. Wu, Z. X. Sun, F. Xu, L. X. Sun, Y. P. Xia, H. L. Peng, X. C. Lin, B. Li, Y. J. Zou, H. L. Chu, P. R. Huang and E. R. Yan, *Colloids Surf. A Physicochem. Eng. Asp.*, 2022, **638**, 128193.

44 Y. Zhou, D. Sheng, X. Liu, C. Lin, F. Ji, L. Dong, S. Xu and Y. Yang, *Sol. Energy Mater. Sol. Cells*, 2018, **174**, 84–93.

45 N. Gao, T. Tang, H. X. Xiang, W. L. Zhang, Y. B. Li, C. L. Yang, T. Xia and X. L. Liu, *Sol. Energy Mater. Sol. Cells*, 2022, **244**, 111831.

46 Z. Y. Wang, W. F. Situ, X. X. Li, G. Q. Zhang, Z. Huang, W. Z. Yuan, C. Z. Yang and C. X. Yang, *Appl. Therm. Eng.*, 2017, **123**, 1006–1012.

47 D. Zhang, B. Zhou, J. Yu, C. E. He, B. Wang, Y. Z. Feng, C. T. Liu and C. Y. Shen, *Composites, Part A*, 2022, **161**, 107128.

48 H. A. Li, R. Y. Lin, L. Q. Zhang, J. Y. Li, C. X. Huang, Y. Y. Wang, P. Y. Chen, R. Q. Liu, Q. W. Dong, Z. Z. Wang and X. W. Wang, *J. Energy Storage*, 2025, **117**, 116220.

49 Y. J. Huo, T. Yan and W. G. Pan, *Sol. Energy*, 2024, **268**, 112269.

50 J. Q. Zhao, X. Wang, X. R. Wang, H. W. Zhao, M. N. Lu, W. Q. Xu, H. E. Nian and J. H. Li, *Chem. Eng. J.*, 2024, **500**, 156922.

51 L. Qiu, K. N. Yan, Y. H. Feng and X. L. Liu, *Energy*, 2023, **278**, 127794.

52 S. Yan, C. Q. Feng, G. H. Yuan, H. H. Wang and H. M. Xu, *J. Energy Storage*, 2025, **114**, 115853.

53 S. Y. Gao, J. Ding, W. L. Wang and J. F. Lu, *Compos. Sci. Technol.*, 2023, **234**, 109945.

54 M. Y. Sun, F. Y. Sun, H. S. Di, C. L. Wu, H. Y. Sheng, L. Lin and Q. Wang, *Mater. Today Sustain.*, 2024, **26**, 100707.

55 Y. Zhang, P. Wu, Y. Meng, R. W. Lu, S. F. Zhang and B. T. Tang, *Chem. Eng. J.*, 2023, **464**, 142650.

56 F. R. Zhang, H. K. Tan, X. L. Lu and W. P. Xuan, *Appl. Therm. Eng.*, 2025, **266**, 125708.

57 L. P. Vandana and R. Ramadoss, *J. Energy Storage*, 2023, **65**, 107258.

58 Y. Li, S. L. Jiang, C. G. Wang and Q. Z. Zhu, *Energy*, 2022, **239**, 122062.

59 H. F. Shi, L. J. Zhang, W. W. Li, X. Han and X. X. Zhang, *Mater. Chem. Phys.*, 2014, **143**, 1069–1074.

60 A. Louanate, R. El Otmani, K. Kandoussi and M. H. Boutaous, *Phys Scripta*, 2020, **95**(10), 105003.

61 X. Chen, H. Y. Gao, G. T. Hai, D. D. Jia, L. W. Xing, S. Y. Chen, P. Cheng, M. Y. Han, W. J. Dong and G. Wang, *Energy Storage Mater.*, 2020, **26**, 129–137.

62 Y. Z. Chen, J. L. Chen, Z. F. Hao, M. S. Selim, J. Yu and X. Chen, *Chem. Eng. J.*, 2023, **463**, 142375.

63 B. Zhao, M. K. Hu, X. Z. Ao, Q. D. Xuan and G. Pei, *Appl. Energy*, 2020, **262**, 114548.